

Electronic supplementary information

Biomimetic Fabrication of Highly Ordered Laminae-trestle-laminae Structured Copper Aero-sponge

Jiankun Huang, Jingbin Zeng*, Hongbin Wang, Ubong J.Etim, Baoqiang Liang, Edem B. Meteku, Honglin Li, Yiyang Wang, Zhiwei Qiu, Mark J. Rood and Zifeng Yan*

Dr. J. Huang, Prof. J. Zeng, Dr. H. Wang, Dr. E. Meteku, Dr. Z. Qiu
College of Science, China University of Petroleum (east), Qingdao, 266580, China
E-mail: zengjb@upc.edu.cn

Dr. B. Liang, Dr. Y. Wang, Dr. H. Li, Prof. Z. Yan
College of Chemical Engineering, China University of Petroleum (east), Qingdao,
266580, China
E-mail: zfyancat@upc.edu.cn

Dr. Ubong J.Etim
College of Chemical Engineering, Guangdong Technion-Israel Institute of Technology,
241 Daxue Road, Jinping District, Shantou, Guangdong Province, China

Dr. Mark J. Rood
Department of Civil and Environmental Engineering, University of Illinois 3230E
Newmark Lab, MC-250, 205 N. Mathews Ave. Urbana, IL 61801 USA

List of Contents

Figure S1. Copper nanowires prepared by hydration hydrazine reduction.

Figure S2. HRTEM images of Laminae-trestle-laminae structure.

Figure S3. Long-ranged and porous microstructure of CNA-20.

Figure S4. XRD results of aero-sponge samples.

Table S1. Effect of PVA dosage on density and Young's modulus of aero-sponges.

Figure S5. Copper aero-sponges with different PVA dosages.

Figure S6. Compression-recovery performance of CNA-40 at the strain of 50%.

Figure S7. 500th cyclic compression tests of CNA-20.

Figure S8. Creep profiles of CNA-20 under a constant stress of 1 kPa and 6 kPa for 30 min.

Figure S9. Cushioning property of dried loofah sponge.

Figure S10. Water-stimulated crimp of planar CuNWs network.

Figure S11. Time-dependent water contact angle variation of CuNW, CNA-x samples and PVA aero-sponge.

Figure S12. Wettability of copper nanowires.

Figure S13. PVA aero-sponge and corresponding wettability.

Figure S14. FT-IR results of aero-sponges.

Figure S15. Wettability of CNA-20 in the radial direction.

Figure S16. Diesel oil droplets spread onto CNA-20 and water droplets stand onto it.

Figure S17. SEM images of conventional freeze-casting aero-sponge.

Figure S18. Total interaction variation in oil-water selective absorption behaviors of hybrid system by MD simulations.

Figure S19. Van der Waals interaction variation in oil-water selective absorption behaviors of hybrid system by MD simulations.

Figure S20. Absorption capacities of loofah stem, activated carbon and conventional freeze-casting aero-sponge.

S1. Mechanisms of Capillary Force-driven Adsorption.

Figure S21. Organic solvent absorption mechanism model.

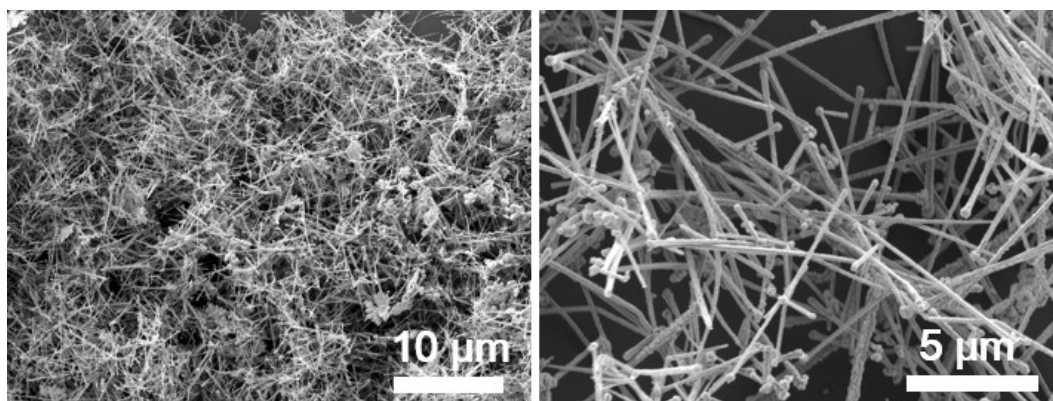


Figure S1. Copper nanowires prepared by hydration hydrazine reduction

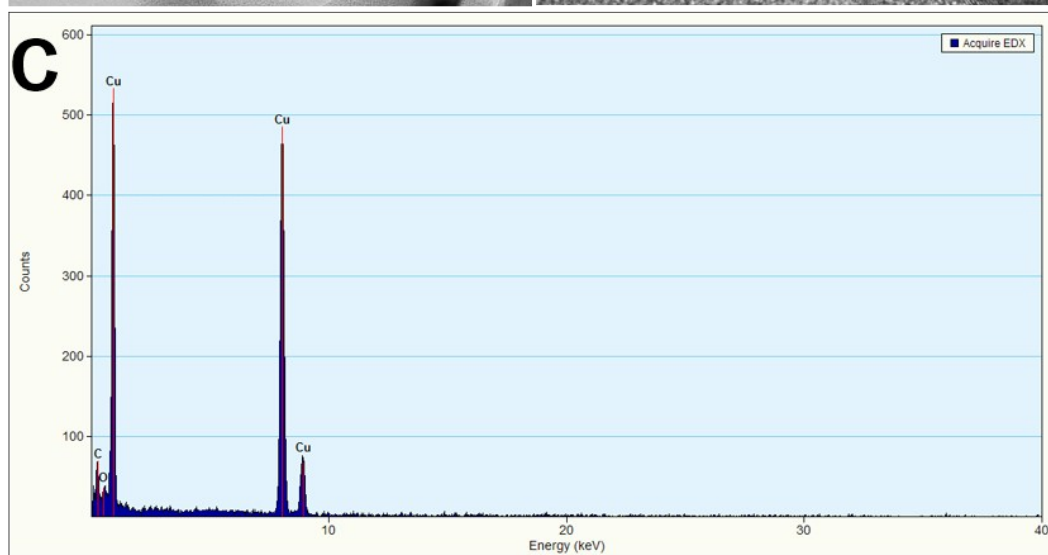
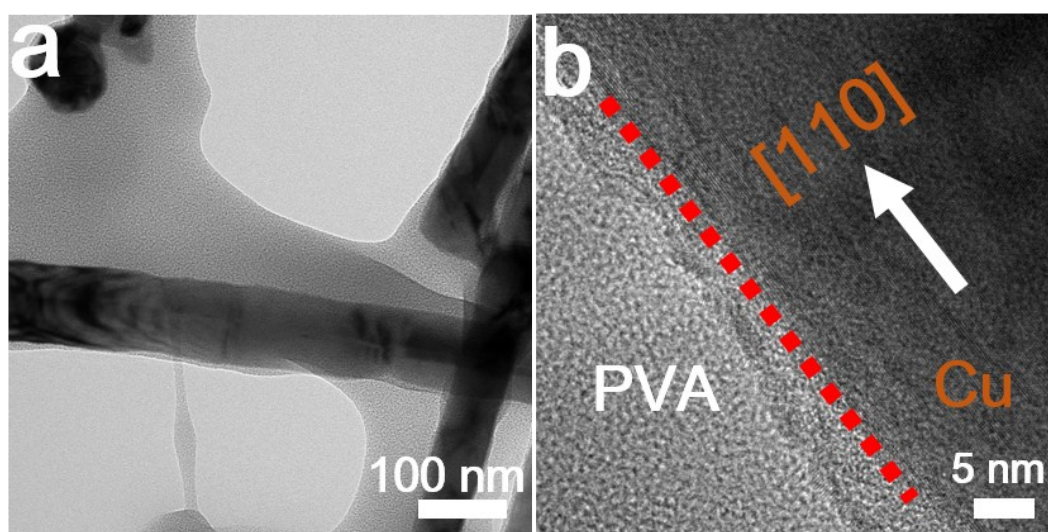


Figure S2. HRTEM images of Laminae-trestle-laminae structure. (a) Copper nanowires were coated by polymer layers. (b) Amplified image of coating state. (c) EDX spectra.

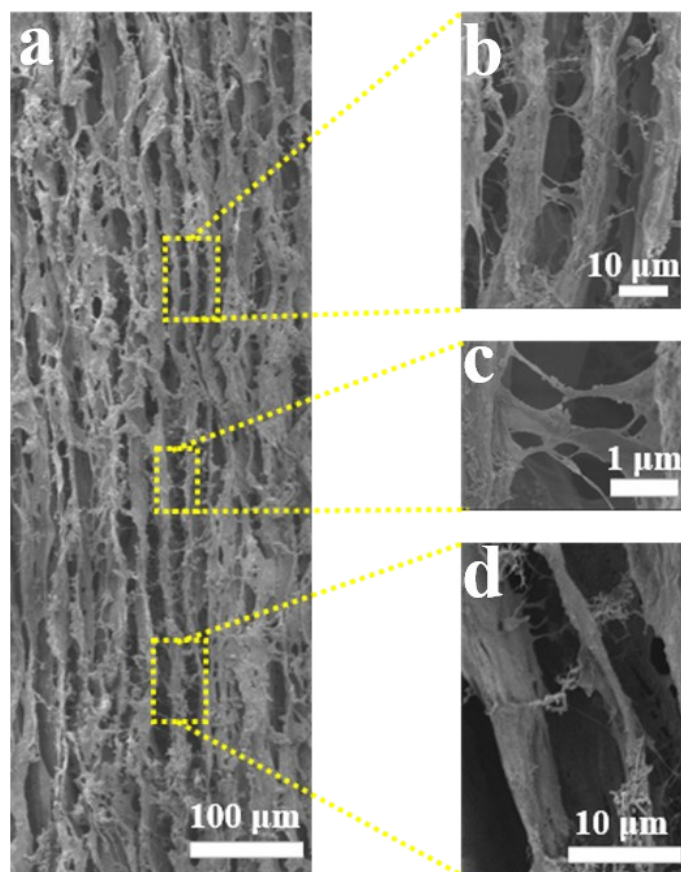


Figure S3. Long-ranged and porous microstructure of CNA-20. (a) SEM images of vertical plane. (b) Magnified SEM image and conceptual proof of interlayers connected by copper nanowires (upper phase). (c) Trestles between layers. (d) Laminae-trestles-laminae structure (bottom).

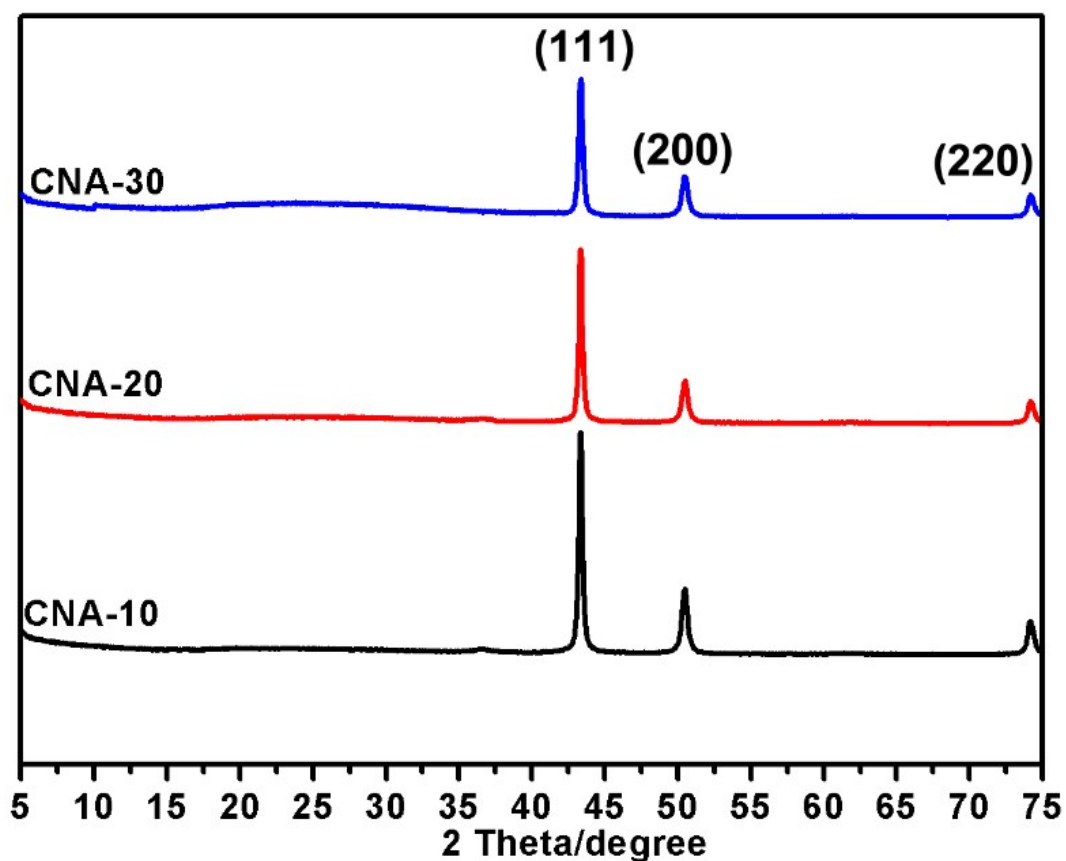


Figure S4. XRD results of aero-sponge samples.

Table S1. Effect of PVA dosage on density and Young's modulus of aero-sponges

No.	CNA-10	CNA-20	CNA-30	CNA-40	CNA-50	CNA-60
Density/ mg cm^{-3}	15.85	21.72	32.48	40.24	53.04	65.12
Young's modulus/ kPa	0.29	0.55	0.25	0.19	0.15	0.09



Figure S5. Copper aero-sponges with different PVA dosages.

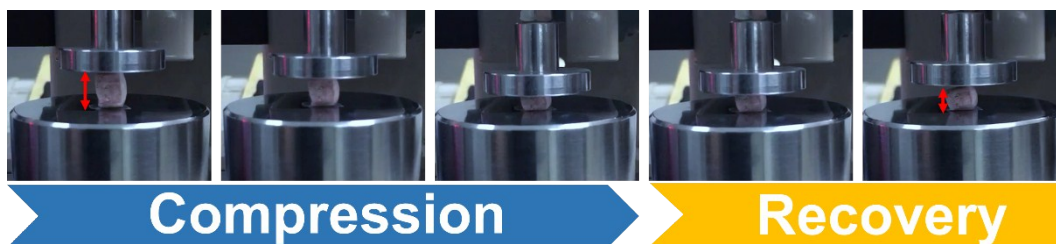


Figure S6. Compression-recovery performance of CNA-40 at the strain of 50%.

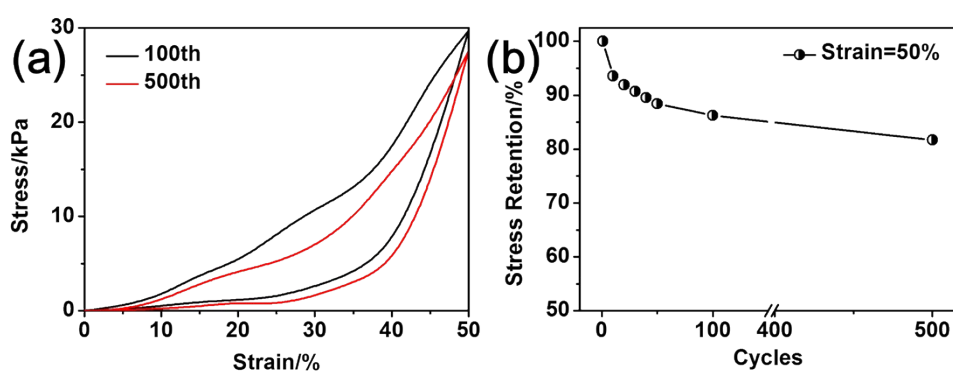


Figure S7. 500th cyclic compression tests. (a) strain-stress curves at 50% compressive strain. (b) Stress retention in cyclic compression tests.

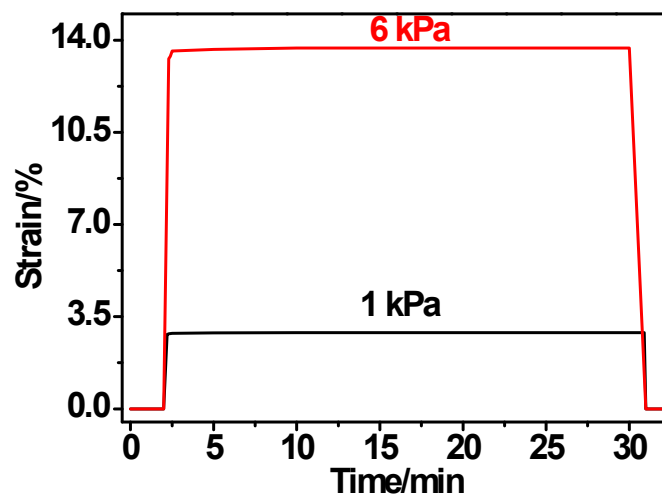


Figure S8. Creep profiles of CNA-20 under a constant stress of 1 kPa and 6 kPa for 30 min.

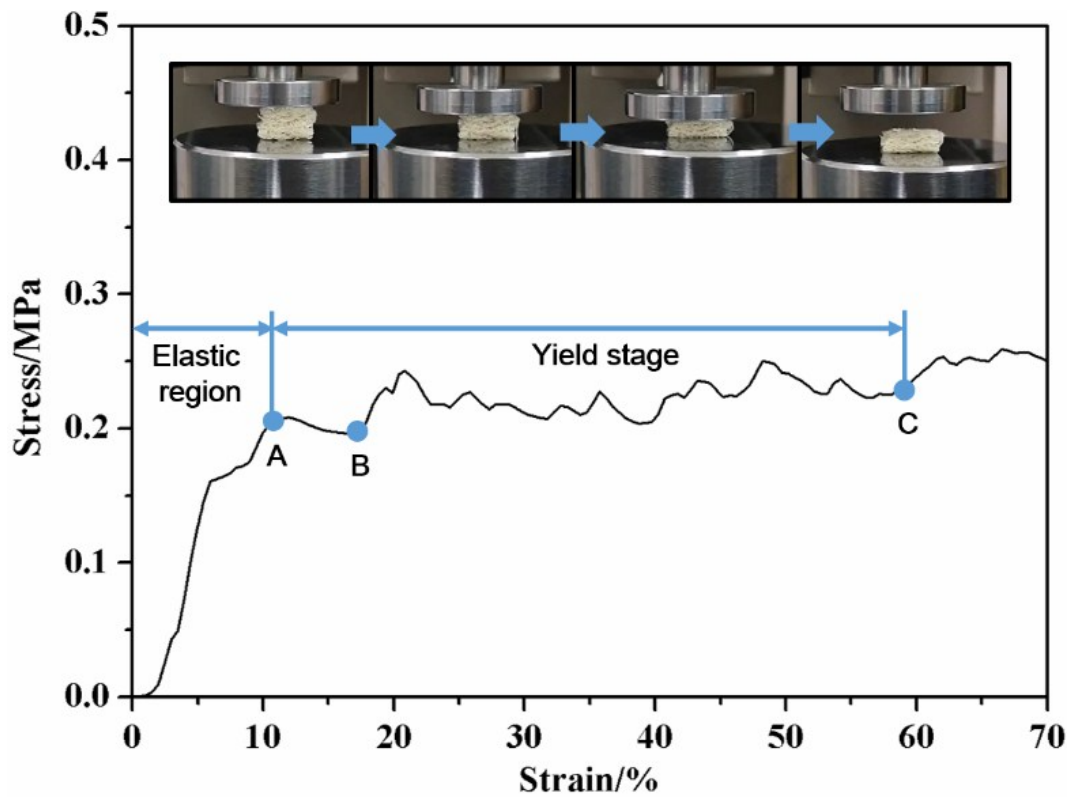


Figure S9. Cushioning property of dried loofah sponge.

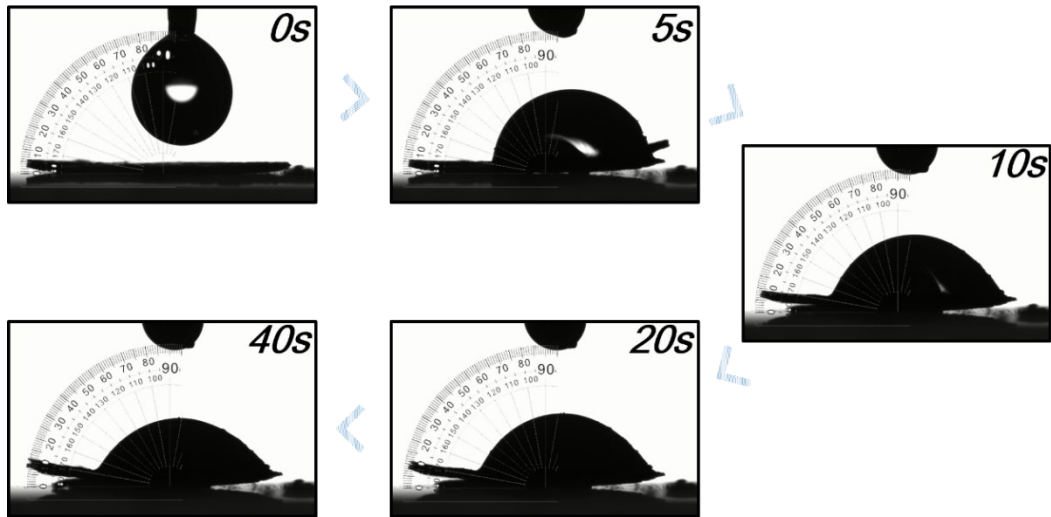


Figure S10. Water-stimulated crimp of planar CuNWs network.

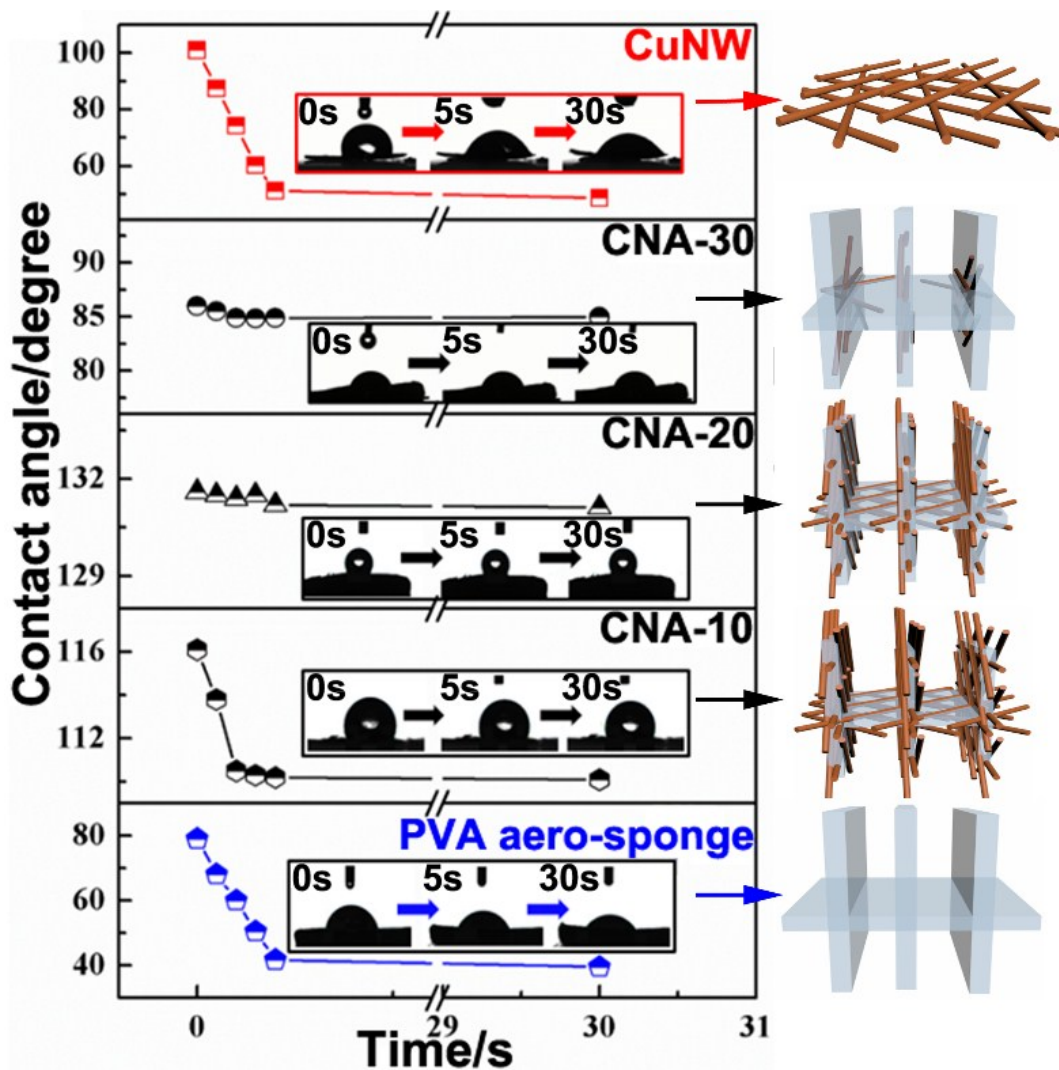


Figure S11. Time-dependent water contact angle variation of CuNW, CNA-x samples and PVA aero-sponge.

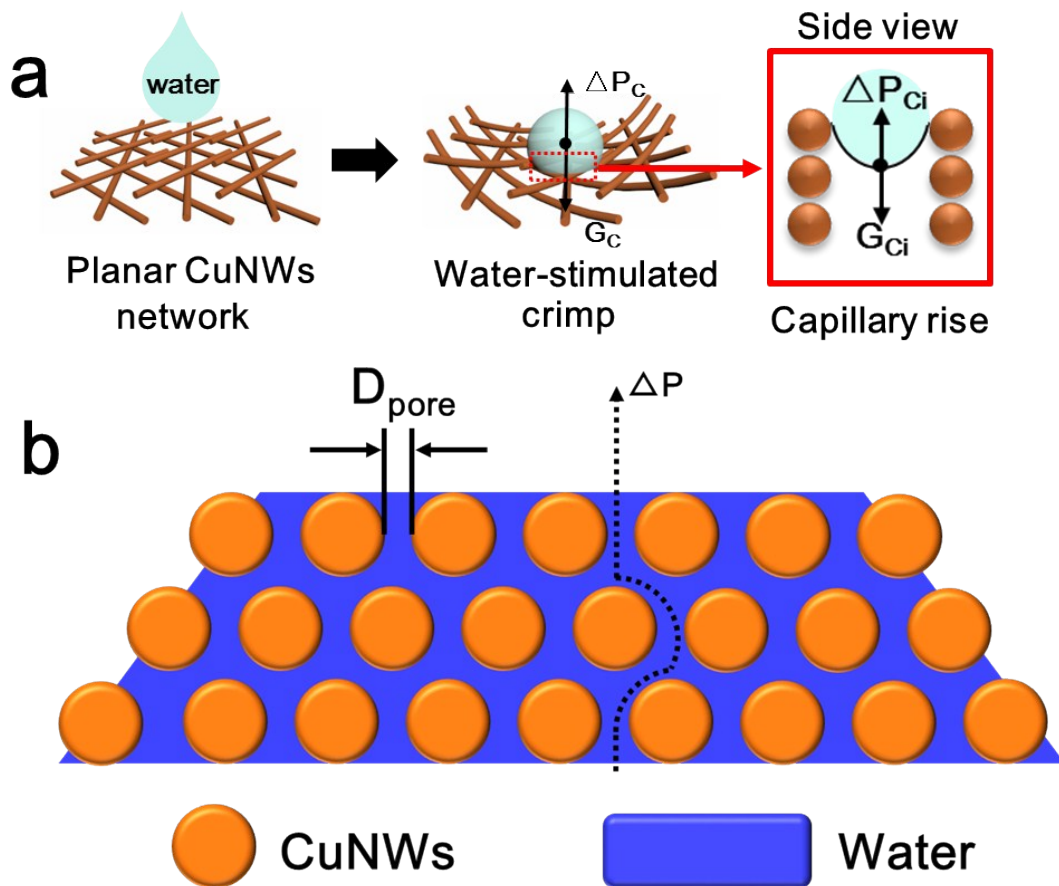


Figure S12. Wettability of copper nanowires. Schematics displaying the response of planar Cu nanowires network under water stimulation. Crimp was formed to prevent water penetration in vertical section. Schematic illustration exhibiting the generated capillary pressure in the CuNWs planar to drive the antigravity water penetration and wide spreading, which is found as a function of pore size.

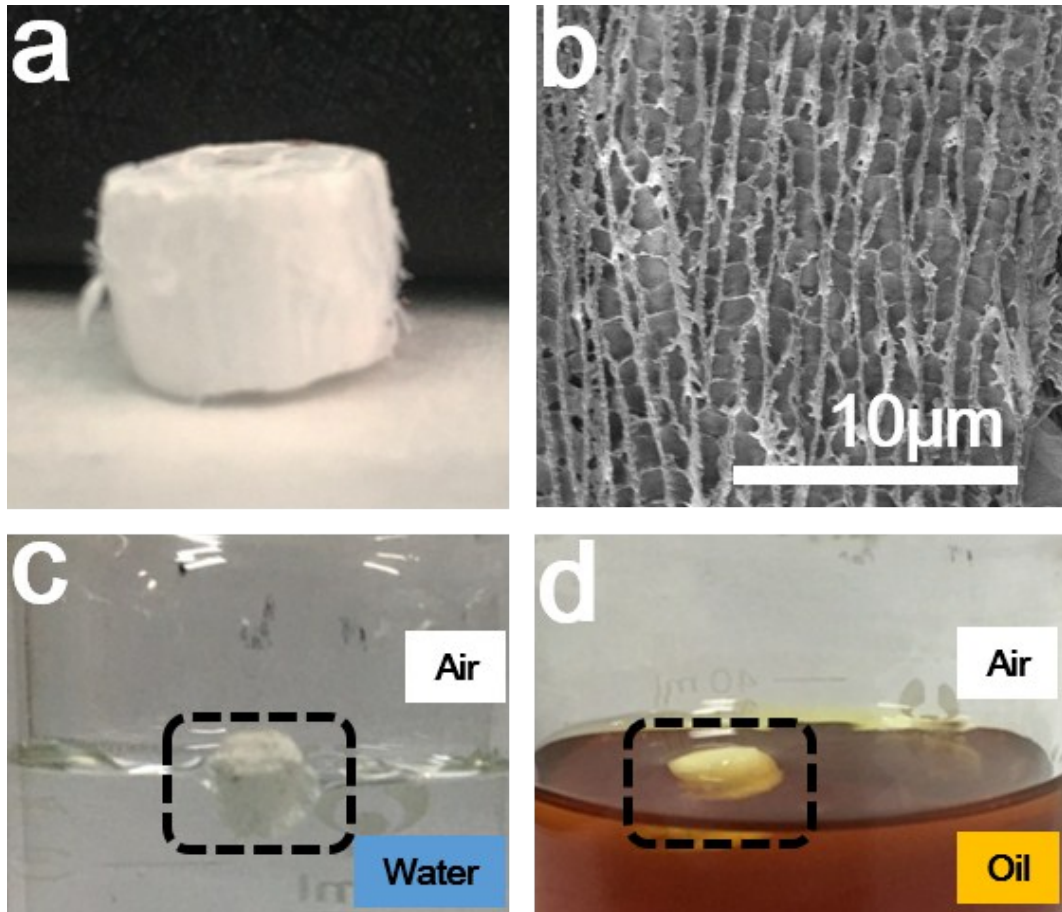


Figure S13. PVA aero-sponge and corresponding wettability. (a) Monolithic shape. (b) SEM image from vertical view. (c) Hydrophilicity of PVA aero-sponge. (d) Hydrophobicity of PVA aero-sponge

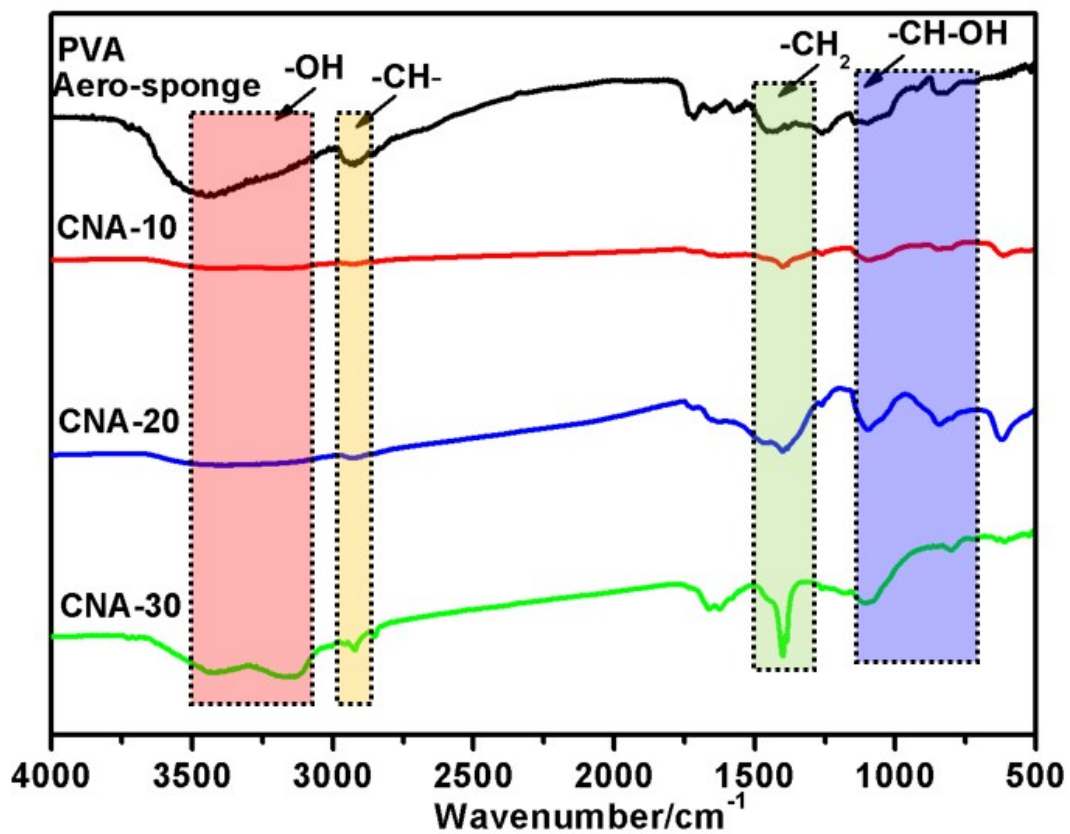


Figure S14. FT-IR results of aero-sponges.

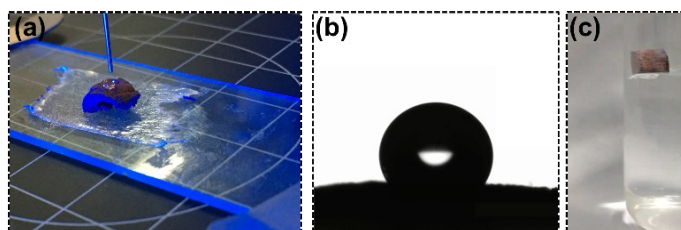


Figure S15. Wettability of CNA-20 in the radial direction. (a) Contact angle measurement (b)

Water Contact angle. (c) CNA-20 lay down on water.

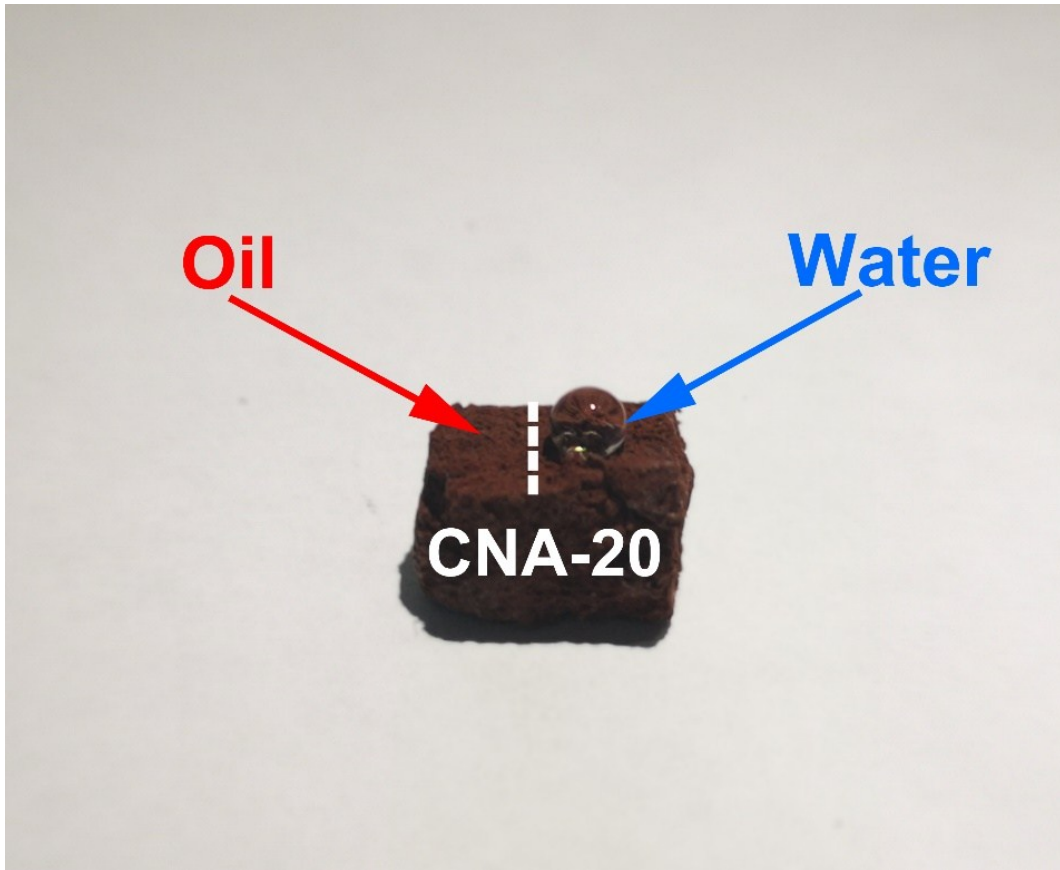


Figure S16. Diesel oil droplets spread onto CNA-20 and water droplets stand onto it.

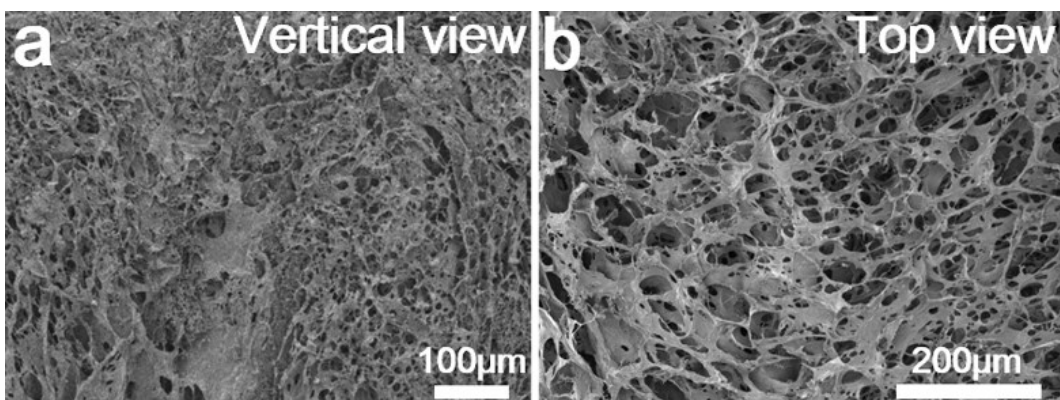


Figure S17. SEM images of conventional freeze-casting aero-sponge (CFA). (a) Vertical view (b) Top view.

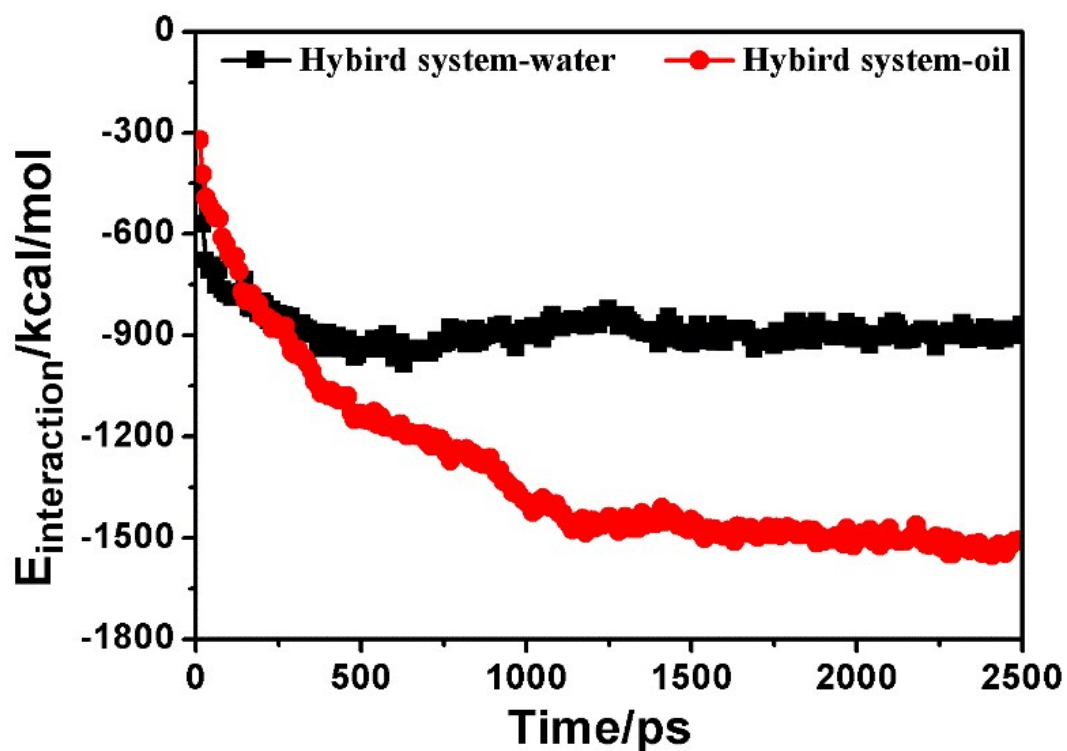


Figure S18. Total interaction variation in oil-water selective absorption behaviors of hybrid system by MD simulations.

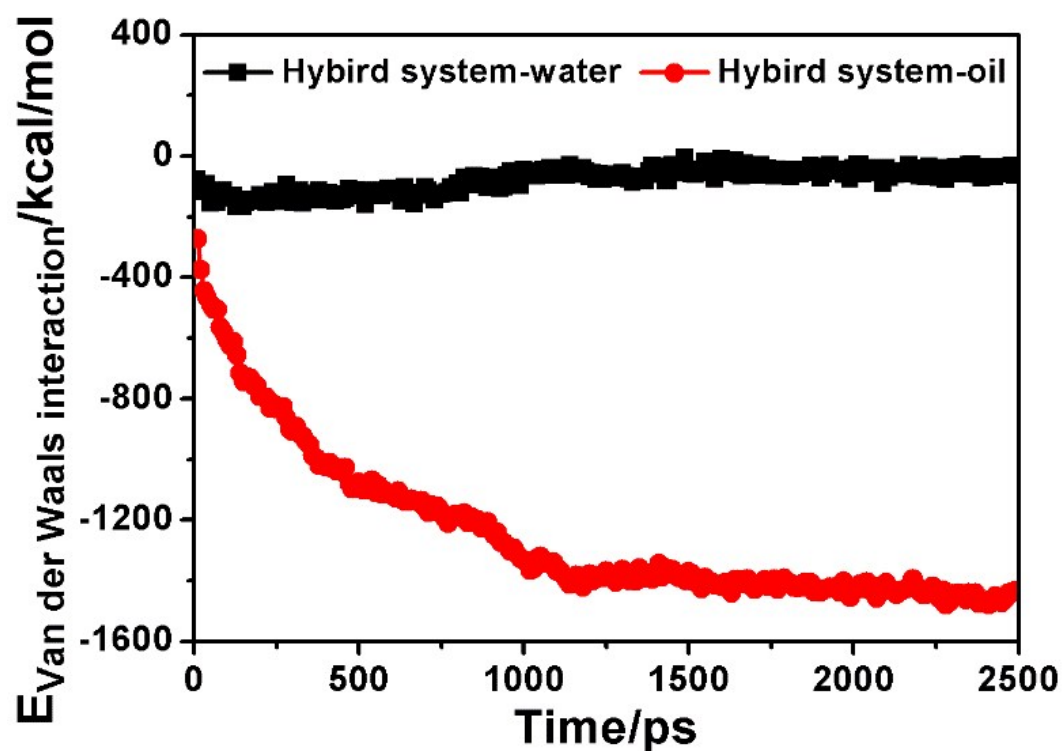


Figure S19. Van der Waals interaction variation in oil-water selective absorption behaviors of hybrid system by MD simulations.

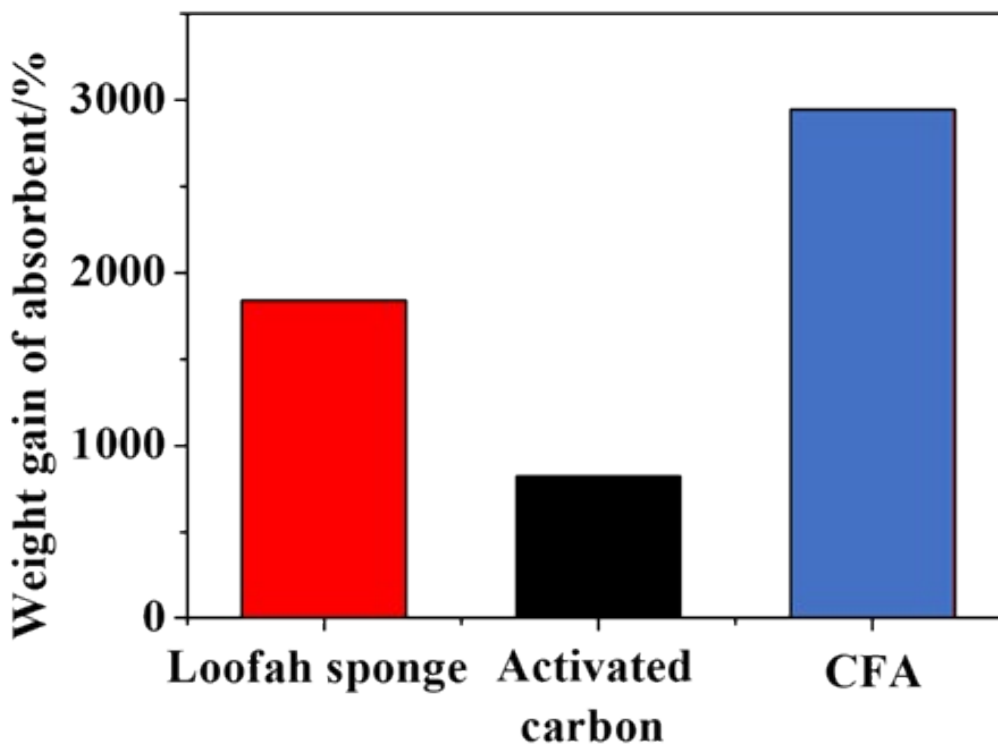


Figure S20. Absorption capacities of loofah stem, activated carbon and conventional freeze-casting aero-sponge.

S1. Mechanisms of Capillary Force-driven Adsorption

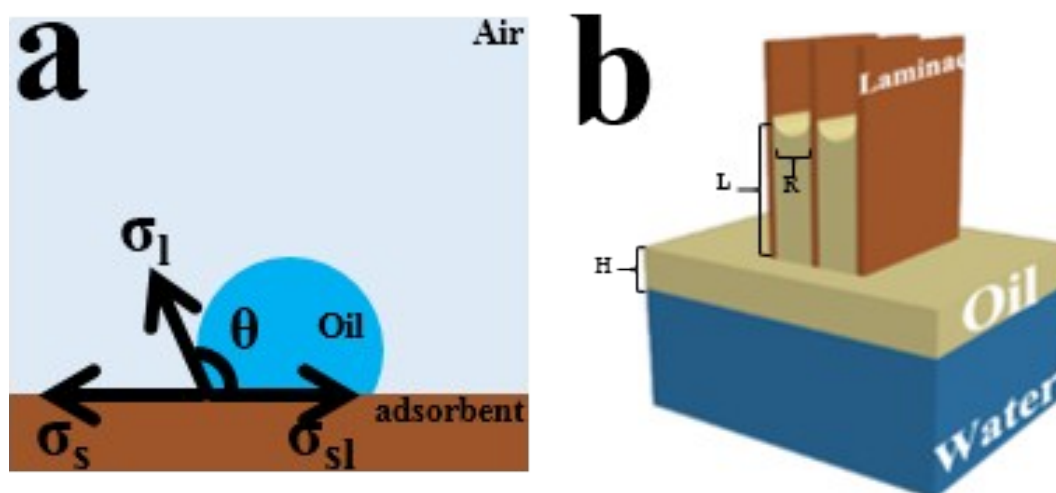


Figure S21. Organic solvent absorption mechanism model. (a) Relationships between interfacial tensions and contact angle (Young's relationship). (b) Directional alignment of capillary flow in CNA-20 with vertical micro-channels.

Under the presumption of constant diesel oil adsorbed volume, the corresponding volume (dV) of oil slicks can be deduced by eq. (S2):

$$V = \frac{\pi R^2 L}{4H} \quad (1.1)$$

Where R is the radius of micro-channels, L is the climbing height of adsorbed oil and H is oil slick width.

For the formation of new interface phase, interfacial adsorption energy ΔG was deduced by the following eq. (S3)¹:

$$\Delta G = V\sigma_{wa} - V(\sigma_{ow} + \sigma_{oa}) + \pi RL(\sigma_{so} - \sigma_{sa}) \quad (1.2)$$

In this equation, σ_{wa} is interfacial tension between water and air², which can be found from the reference, σ_{ow} and σ_{oa} are the oil-water and oil-air interfacial tension, respectively, which were measured by DSA-30.

Table. S2. Interfacial tensions used for mechanism deduction(T=25°C)

Interfacial Tension No.	Name	Interfacial tension (N m ⁻¹)
1	σ_{wa}	7.2×10^{-2}
2	σ_{ow}	2.6×10^{-2}
3	σ_{oa}	3.3×10^{-2}

Besides, according to Young's equation, σ_{sa} could be derived as the followed form (eq. S4),

$$\sigma_{sa} = \sigma_{so} + \sigma_{oa} \cos \theta \quad (1.3)$$

Thus, eq. (S2) can be modified as followed,

$$\Delta G = A\sigma_{wa} - A\sigma_{ow} - A\sigma_{oa} - \frac{4AH}{R} \cos \theta \sigma_{oa} \quad (1.4)$$

The $\cos \theta$ equals approximately to 1 due to spreading behavior of oil on CNA-20. Results from eq. 1.4 reveals that, if H was 0.09 times greater than R, the absorption free energy ΔG would show a tendency of reduction. As shown in Figure S3, the radius of CNA-20 ranges from 8 μm ~20 μm , so it is quite easy to found that $H > 0.09R$. In this case, the whole adsorption process is a spontaneous one.

References

- 1 A .Adamson, *Phys. Chem. of surf.* Wiley, 1990.
- 2 Dean J A . Lange's handbook of Chemistry. *Advanced Manufacturing Processes*, 1990, 5(4):2.